Article:

Karthikeyan, Sekar, Ahmed, Kassam, Osatiashtiani, Amin et al. (2020) Pompon Dahlia-like Cu2O/rGO Nanostructures for Visible Light Photocatalytic H2 Production and 4-Chlorophenol Degradation. ChemCatChem. ISSN: 1867-3899

https://doi.org/10.1002/cctc.201902048

Pompon Dahlia-like Cu_2O/rGO nanostructures for visible light photocatalytic H_2 production and 4-chlorophenol degradation

Sekar Karthikeyan,*[a],[b] Kassam Ahmed,[a] Amin Osatiashtiani,[a] Adam F. Lee,*[c] Karen Wilson,[c] Keiko Sasaki,[b] Ben Coulson,[d] Will Swansborough-Aston,[d] Richard E. Douthwaite,[d] and Wei Li*[a]

Abstract: Hierarchical Cu_2O nanospheres with a Pompon Dahlia-like morphology were prepared by a one-pot synthesis employing electrostatic self-assembly. Nanocomposite analogues were also prepared in the presence of reduced graphene oxide (rGO). Photophysical properties of the hierarchical Cu_2O nanospheres and Cu_2O/rGO nanocomposite were determined, and their photocatalytic applications evaluated for photocatalytic 4-chlorophenol (4-CP) degradation and H_2 production. Introduction of trace (<1 wt%) rGO improves the apparent quantum efficiency (AQE) at 475 nm of hierarchical Cu_2O for H_2 production from 2.23 % to 3.35 %, giving an increase of evolution rate from 234 $\mu mol.g^{-1}.h^{-1}$ to 352 $\mu mol.g^{-1}.h^{-1}$ respectively. The AQE for 4-CP degradation also increases from 52 % to 59 %, with the removal efficiency reaching 95 % of 10 ppm 4-CP within 1 h. Superior performance of the hierarchical Cu_2O/rGO nanocomposite is attributable to increased visible light absorption, reflected in a greater photocurrent density. Excellent catalyst photostability for >6 h continuous reaction is observed.

Introduction

Global energy and health challenges arising from anthropogenic fossil fuel usage (and resulting climate change) and contamination of aquatic environments are driving the development of environmentally benign technologies for energy production/storage and wastewater treatment.[1] Solar energy has emerged as a key resource to address such challenges,[2] both through direct electric power generation, and harnessing by semiconductor photocatalysts for aqueous phase H_2 evolution, CO_2 reduction and pollutant degradation, and antimicrobial coatings.[3]

Many transition metal oxide semiconductors possess tunable bandgaps and favourable conduction and valence band energies to efficiently separate photoexcited electron(e^-)-hole(h^+) pairs.[4] Significant research effort has focused on strategies to tune the photophysical properties of oxide semiconductors by modifying their surface/interface properties through crystal facet engineering, the formation of phase junctions or heterojunctions, and the incorporation of co-catalysts, with the goal of efficient solar light harvesting and improved charge carrier separation/energy matching (and hence high activity and selectivity) to the selected reactant and desired product.[5] Copper (I) oxide is an abundant and low-cost p-type semiconductor with a direct (forbidden) band gap of 2.17 eV and optical band gap of 2.62 eV,[6] which is favourable for overall photocatalytic water splitting to produce H_2 under visible light ($\lambda \leq 600$ nm) irradation.[7] Cu_2O has a high optical absorption coefficient, with a high theoretical H_2 conversion efficiency of 18 % for water splitting,[8] and power conversion efficiency of 20 %, and hence finds widespread application in photocatalysis environmental pollutant remediation[9] and solar cells.[10] However, the reduction and oxidation potentials of Cu_2O lie within its bandgap resulting in poor photostability,[8] and rapid recombination of photogenerated charge carriers occurs.[11]

Various structural modifications of Cu_2O have been investigated to overcome these limitations, with different morphologies such as nano-wires[12], cubes[13], flowers,[14] and spheres,[15] offering significant improvements in photophysical properties for photocatalytic applications. Size and morphology of Cu_2O nanostructures determine their resulting chemical and physical properties.[16] Hierarchical semiconductors have gained recent interest as they can offer additional control of electronic and optical properties.[17] We reported a hierarchical Cu_2O photocatalyst comprised of individual nanoparticles assembled into porous nanocubes that exhibited a promising hydrogen productivity (water splitting) 15 $\mu mol\ g^{-1}.h^{-1}$ corresponding to an apparent quantum efficiency (A.Q.E) of 1.2 % in the presence of a Pt co-catalyst.[18] Hierarchical structures also offer improved mass transport to confer higher photocatalytic activity,[19] although existing fabrication routes often employ disposable templates, high temperatures (170 °C),[20] and/or coatings, which increase catalyst production cost and time.[21]

Graphene is a two dimensional monolayer of sp^2 hybridised carbon atoms, which due to its unique physical and electronic properties, has attracted global scientific interest and investment since its formal discovery/isolation in 2004.[22] The reduced form of the oxide of graphene, reduced graphene oxide (rGO), exhibits a high surface area, tunable band gap, and excellent electron mobility.[23] rGO surfaces also possess a variety of chemically reactive oxygen functionalities that render it a versatile catalyst support and amenable to mixing with other semiconductors to form hybrid semiconductor composites with potentially superior photocatalytic properties.[24] Indeed, graphite and rGO nanosheets have been explored as supports for dispersing Cu_2O

---

[a] Dr S. Karthikeyan, K. Ahmed, Dr A. Osatiashtiani, Dr W. Li
European Bioenergy Research Institute
Aston University
Birmingham B4 7ET (UK)
E-mail: karthik.keyan02@gmail.com; w.li8@aston.ac.uk
[b] Dr S. Karthikeyan, Prof K. Sasaki
Department of Earth Resources Engineering
Kyushu University
Fukuoka 819-0395 (Japan)
[c] Prof A.F. Lee, Prof K. Wilson
RMIT University
Melbourne VIC3000 (Australia)
E-mail: adam.lee2@rmit.edu.au
[d] Dr B. Coulson, W. Swansborough-Aston, Dr R.E. Douthwaite
Department of Chemistry
University of York
York YO10 5DD (UK)

Supporting information for this article is given via a link at the end of the document.

and TiO_2 respectively. Carbonaceous supports are reported to facilitate photoexcited charge separation, and hence improve the photocatalytic activity and photostability of Cu_2O,[9a, 25] while thin protective carbon layers arising from glucose carbonisation can significantly increase the photocurrent density and photostability of Cu_2O for photoelectrochemical water splitting.[26]

Herein we report the one-pot hydrothermal synthesis and photocatalytic application of hierarchical Cu_2O nanospheres and corresponding Cu_2O/rGO nanocomposites for 4-chlorophenol (4-CP) degradation and H_2 production under visible light. 4-CP was selected as a hazardous, recalcitrant organic compound present in waste water effluent from diverse industrial processes (e.g. pulp and paper, textile and petroleum sectors), and unlike organic dyes does not act as a catalyst photosensitiser. Intermixing rGO and hierarchical Cu_2O nanospheres improved photocatalytic activities (and apparent quantum efficiencies) for both reactions relative to the nanospheres alone, without requiring a precious metal co-catalyst or external bias, associated with improved visible light absorption by the nanocomposite. In addition, photodegradation of 4-CP favoured less toxic organic oxidation products

Results and Discussion

Structure, photophysical and electronic properties

The synthetic route to Pompon Dahlia-like Cu_2O/rGO is illustrated in **Scheme 1**. The Cu(II)-PEG complex was added to graphene oxide to form a hybrid inorganic-organic nanostructure wherein polar groups on the graphene oxide nanosheets promote multivalent bridging (via hydrogen bonding) of GO with ligand coordinated Cu^{2+} ions. Subsequent hydrazine reduction in the presence of NaOH likely promotes a transition from ion-by-ion growth to particle-mediated crystallization of complexed Cu(I) ions in parallel with reduction of the graphene framework[27] to form a hierarchical Cu_2O/rGO nanocomposite. PEG likely acts as a structure-directing agent promoting the formation of discrete Cu_2O nanoparticles which coalesce at the rGO surface. Transformation of Cu_2O agglomerates into hierarchical structure may proceed by Ostwald ripening and/or self-aggregation and the simultaneous reduction of GO yielding an integrated nanocomposite. A related (albeit template-free) aggregation of hollow Cu_2O microstructures via hydrazine reduction is reported in the literature, however neither the photophysical properties nor catalytic performance were described.[28]

The morphologies of hierarchical Cu_2O and the Cu_2O/rGO nanocomposite were examined by TEM and SEM (**Figure 1** and **2**). TEM of hierarchical Cu_2O shows ~400-500 nm aggregates of spherical Cu_2O nanoparticles (mean size ~50 nm) in good agreement with SEM images **(Figure S1)**.

Corresponding TEM images of the hierarchical Cu_2O/rGO nanocomposite also present semi-transparent graphene oxide sheets that exhibit folds and wrinkles (**Figure 2a-d**) which are in intimate contact with the Cu_2O aggregates possibly driven by electrostatic interactions arising from reduction of the parent graphene oxide.[29] Cu_2O aggregates and individual particles in the nanocomposite were slightly smaller than those of the free hierarchical Cu_2O, being 250-400 nm (**Figure 2a** inset) and 15-30 nm (**Figure 2c** inset) respectively. Aggregates still exhibited a Pompon Dahlia-like morphology (**Figure 2b** inset and **Figure S1**).

Phase analysis by XRD confirmed the exclusive formation of crystalline Cu_2O (**Figure 3a**) in the hierarchical Cu_2O and Cu_2O/rGO nanocomposite, indicated by peaks at 29.56°, 36.41°, 42.31°, 61.36°, and 73.50° associated with characteristic (110), (111), (200), (220), (311), and (222) reflections of pure Cu_2O phase (JCPDS 03-0898)[30] and lattice constants a=5.19; b=5.08, c=11.69 and β=90.38. The absence of reduced graphene oxide

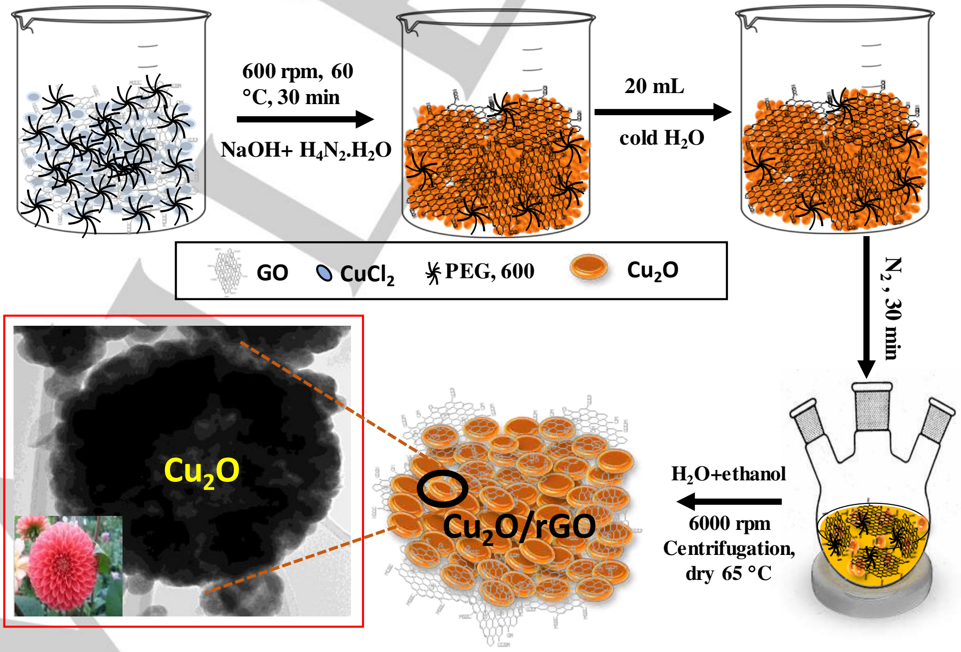

Scheme 1. Synthesis of a Pompon Dahlia-like Cu_2O/rGO nanocomposite photocatalyst.

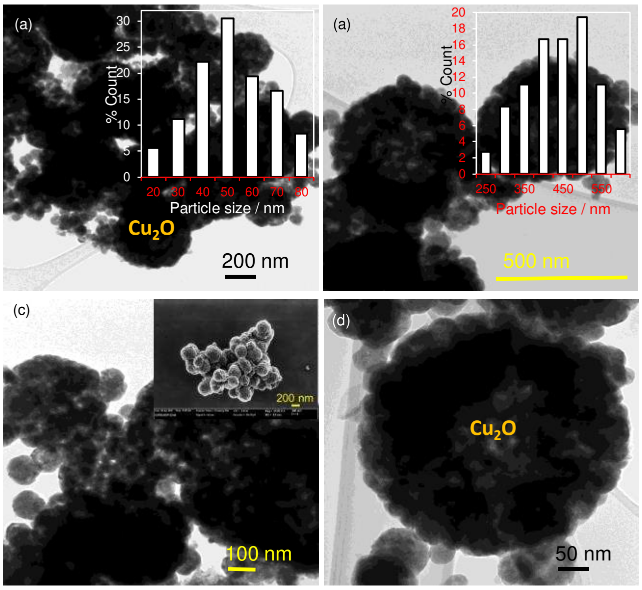

Figure 1. (a-d) TEM images of Pompon Dahlia-like hierarchical Cu_2O. Insets show particle size distributions (a) for the individual Cu_2O nanoparticles and (b) for the aggregates, and (c) a corresponding SEM image of the aggregates.

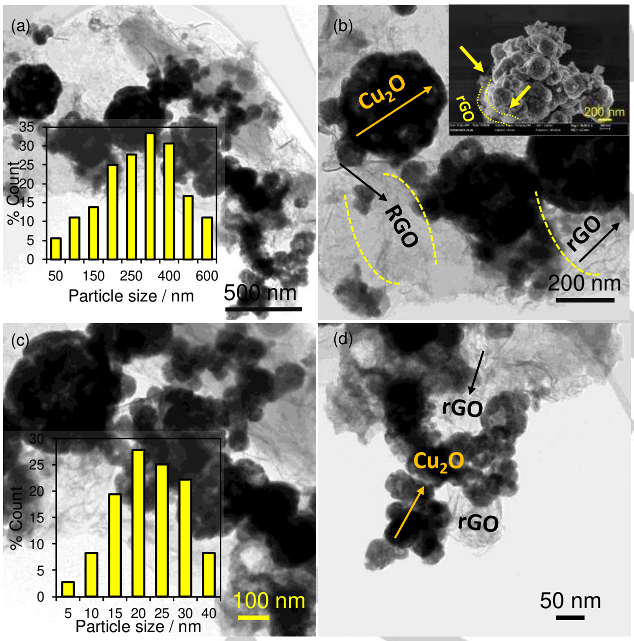

Figure 2. (a-d) TEM images of Pompon Dahlia-like hierarchical Cu_2O/rGO nanocomposite. Insets show particle size distributions (a) for the aggregates and (c) for individual Cu_2O nanoparticles, and (b) a corresponding SEM image and (d) high resolution TEM image of the aggregates.

reflections ~25 ° peaks is ascribed to its very low concentration (<0.4 wt%) in the nanocomposite.[31] Volume-averaged crystallite sizes calculated from the Scherrer equation reveal similar (15 nm) Cu_2O nanoparticles for both materials, suggesting the rGO matrix exerts little impact on the precipitation and reduction of the copper precursor. Textural properties of the hierarchical Cu_2O and Cu_2O/rGO nanocomposite revealed identical, low BET surface areas of 13 $m^2.g^{-1}$ (**Table 1**) comparable to those previously reported for single crystal Cu_2O-rGO composites,[32] and identical BJH pore size distributions (**Figure S2**) indicative of ~2 nm mesopores presumably associated with voids between individual Cu_2O nanoparticles in the aggregates. The mesopore volume of the nanocomposite was similar to that of the hierarchical Cu_2O. Optical absorption properties of the two materials were studied by DRUVS (**Figure 3b**); although both exhibited broad absorbance between 200-600 nm consistent with literature reports,[32-33] the band edge of the Cu_2O/rGO nanocomposite was red-shifted. Optical band gaps *Eg* were calculated from the corresponding Tauc plots (**Figure 3c**) using **Eq. 4**:

$$\alpha hv = A(hv - E_g)^n \qquad \textbf{4}$$

where *A* is the absorption coefficient and α the linear absorption coefficient determined from the Kubelka-Munk formalism in **Eq. 5**:

$$a = \frac{(1-R)^2}{2R} \qquad \textbf{5}$$

The resulting direct band gaps were 2.42 eV and 2.13 eV for hierarchical Cu_2O and the Cu_2O/rGO nanocomposite respectively. Since rGO shows weak adsorption >400 nm,[34] the red shift in the nanocomposite must arise from interfacial contact between rGO sheets and Cu_2O and a change in the oxide valence band (VB) and/or conduction band (CB) energies, as previously reported.[35] Such band gap narrowing increase light absorption which could enhance visible light photocatalysis.[32] Note that the Cu_2O band gap is reported to vary between 2.1-2.6 eV, being sensitive to quantum confinement effects and heterojunction formation.[10, 36]

Table 1. Photophysical properties of Pompon Dahlia-like hierarchical Cu_2O and Cu_2O/rGO nanocomposite.

Sample	Crystal size[a] / nm	Particle size[b] / nm	BET area[c] / $m^2.g^{-1}$	Band gap[d] / eV	CB edge[e] / eV	VB edge[e] / eV
Hierarchical Cu_2O	15.3	400-500	13	2.42	-1.12	+1.3
Hierarchical Cu_2O/rGO	14.7	250-400	13	2.13	-1.03	+1.1

[a] XRD. [b] TEM. [c] N_2 porosimetry. [d] DRUVS. [e] Calculated from valence band XPS and DRUVS.

The surface copper oxidation state was quantified from high resolution Cu 2p XP spectra (**Figure 4a**), with the hierarchical Cu_2O and Cu_2O/rGO nanocomposite dominated by spin-orbit split doublets with $2p_{3/2}$ binding energies of 932.2 eV and 934.4 eV indicative of Cu_2O and Cu(II) carbonate dihydroxide respectively, and a weak shake-up satellite at 943.4 eV associated with Cu(II) species. The absence of Cu(II) XRD features suggests that $Cu_2(OH)_2CO_3$ arises from the post-synthetic reaction of Cu_2O nanoparticle surfaces with the surrounding atmosphere.[37]

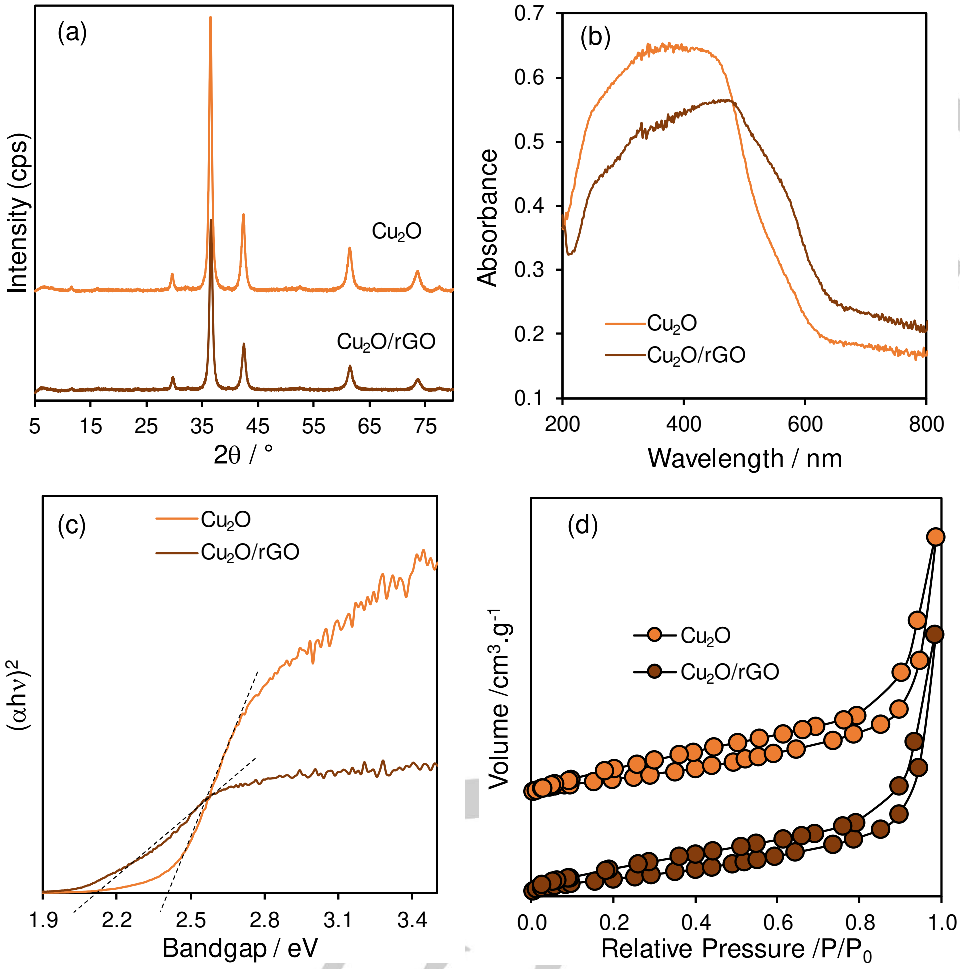

Figure 3. (a) XRD patterns, (b) DRUV spectra and (c) corresponding Tauc plots, and (d) N_2 adsorption-desorption isotherms of Pompon Dahlia-like hierarchical Cu_2O and Cu_2O/rGO nanocomposite.

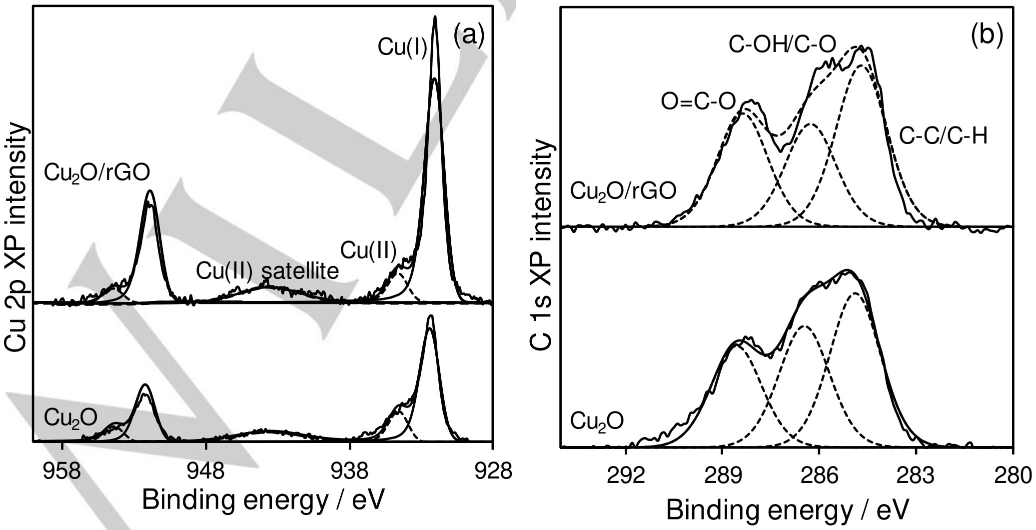

Figure 4. (a) Cu 2p and (b) corresponding C 1s XP spectra of Pompon Dahlia-like hierarchical Cu_2O and Cu_2O/rGO nanocomposite.

Spectral fitting reveals that the surfaces of both hierarchical materials predominantly comprise Cu_2O (**Table S1**) with that of the nanocomposite somewhat enriched (88 % versus 79 %). Corresponding C 1s XP spectra revealed almost identical distributions of three distinct chemical environments for both hierarchical materials at 284.6, 286.2, and 288.3 eV **(Figure 4b),** respectively assigned to the alcohol and ether functions of PEG and surface carbonate.[9a, 38] A small increase in the sp^2 carbon environment was observed for the Cu_2O/rGO nanocomposite consistent with graphene incorporation **(Table S2)**.[37] O 1s spectra were consistent with these assignments, exhibiting three distinct chemical environments at 531.4, 533.4, and 535.8 eV arising from Cu_2O, carbonate, and PEG ether species **(Figure S3)**, with an enhanced Cu_2O contribution for the nanocomposite consistent with a higher Cu(I):Cu(II) atomic ratio and less surface carbonate.

Charge carrier separation and hence photocatalytic performance depend on the electronic band structure, band alignment and interfacial contact of photocatalysts.[39] Band energies were investigated by valence band XPS (**Figure S4a-c**); the VB potential maxima of hierarchical Cu_2O and the Cu_2O/rGO nanocomposite were +1.30 and +1.10 eV respectively relative to the Fermi level, and corresponding CB minima edges (derived from the optical band gap and valence band XP spectra) were -1.12 eV and -1.03 eV for Cu_2O/rGO. The CB minimum is therefore unaffected by formation of the Cu_2O/rGO heterojunction, albeit more negative than previous reports (e.g. -0.42 for oxygen-deficient Cu_2O nanoparticles[40]), and in both cases much greater than required for photocatalytic hydrogen production from water (−0.65 eV at pH 7).[41]

Photocatalytic H_2 production

The photocatalytic activity of the hierarchical Cu_2O and Cu_2O/rGO-0.4 wt% nanocomposite for H_2 evolution for sacrificial water splitting was assessed under visible light irradiation in the presence of methanol as a sacrificial hole scavenger (**Figure 6a-b**). No evolved oxygen was observed for either catalyst. Hydrogen productivities of 18 $\mu mol.g^{-1}.h^{-1}$ and 31 $\mu mol.g^{-1}.h^{-1}$ were measured for the hierarchical Cu_2O and Cu_2O/rGO nanocomposite respectively, with negligible deactivation during 14 h operation. Increasing the methanol concentration to 10 vol% conferred an almost quantitative increase in H_2 productivity, which reached 234 $\mu mol.g^{-1}.h^{-1}$ for the hierarchical Cu_2O and 352 $\mu mol.g^{-1}.h^{-1}$ for the hierarchical Cu_2O/rGO nanocomposite, suggesting that charge carrier recombination is rate-determining for hydrogen evolution over both materials. The greater activity of the nanocomposite equates to an apparent quantum efficiency (AQE) of 3.35 % versus 2.23 % for the hierarchical Cu_2O **(Figure S5**). Interfacing the Cu_2O semiconductor with rGO nanosheets to form a heterojunction almost doubles the specific activity, consistent with greater visible light absorption.[42] Hydrogen production over the hierarchical Cu_2O was superior to that of non-porous (13 $\mu mol.g^{-1}.h^{-1}$)[43] and Cu_2O nanoparticles (10 $\mu mol.g^{-1}.h^{-1}$)[7] of comparable size, and the AQE. higher than reported for Pt-decorated 500 nm Cu_2O nanocubes (AQE = 1.2 %),[41b] 375 nm hierarchical Cu_2O nanocubes (AQE = 1.2 %),[44] and Pt-free 300-500 nm Cu_2O powder (AQE = 0.3 %)[7] and 150 nm Cu_2O nanostructures on a silicon wafer (AQE in water = 0.3 %) under visible light,[45] demonstrating advantageous photophysical properties of our Pompom Dahlia-like aggregates. Hydrogen production over various Cu_2O photocatalysts is summarised in **Table S3**.

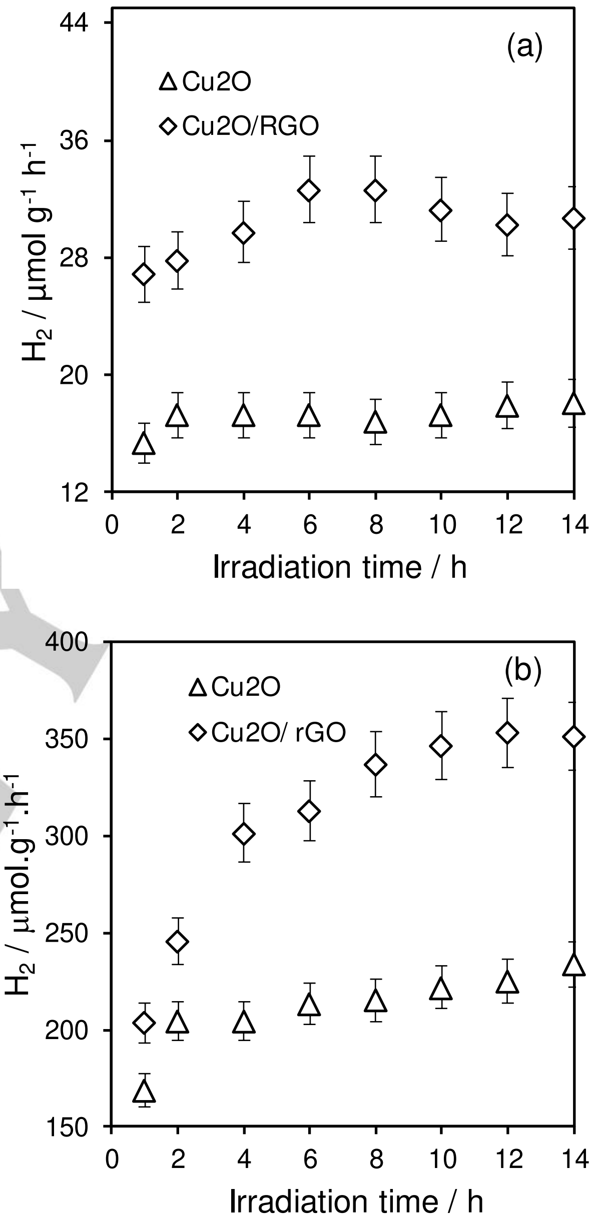

Figure 5. Visible light photocatalytic H_2 production over Pompon Dahlia-like hierarchical Cu_2O and Cu_2O/rGO nanocomposite with (a) 1 vol% and (b) 10 vol% methanol in water as a sacrificial hole scavenger. Reaction conditions: 0.02 g catalyst, 200 W Hg-Xe (λ>420 nm).

Photocatalytic 4-CP removal

Visible light photocatalytic degradation of 4-CP was subsequently studied over the Pompon Dahlia-like hierarchical Cu_2O and Cu_2O/rGO nanocomposite (**Figure S6**). 4-CP was selected as a model recalcitrant organic compound that does not exhibit visible

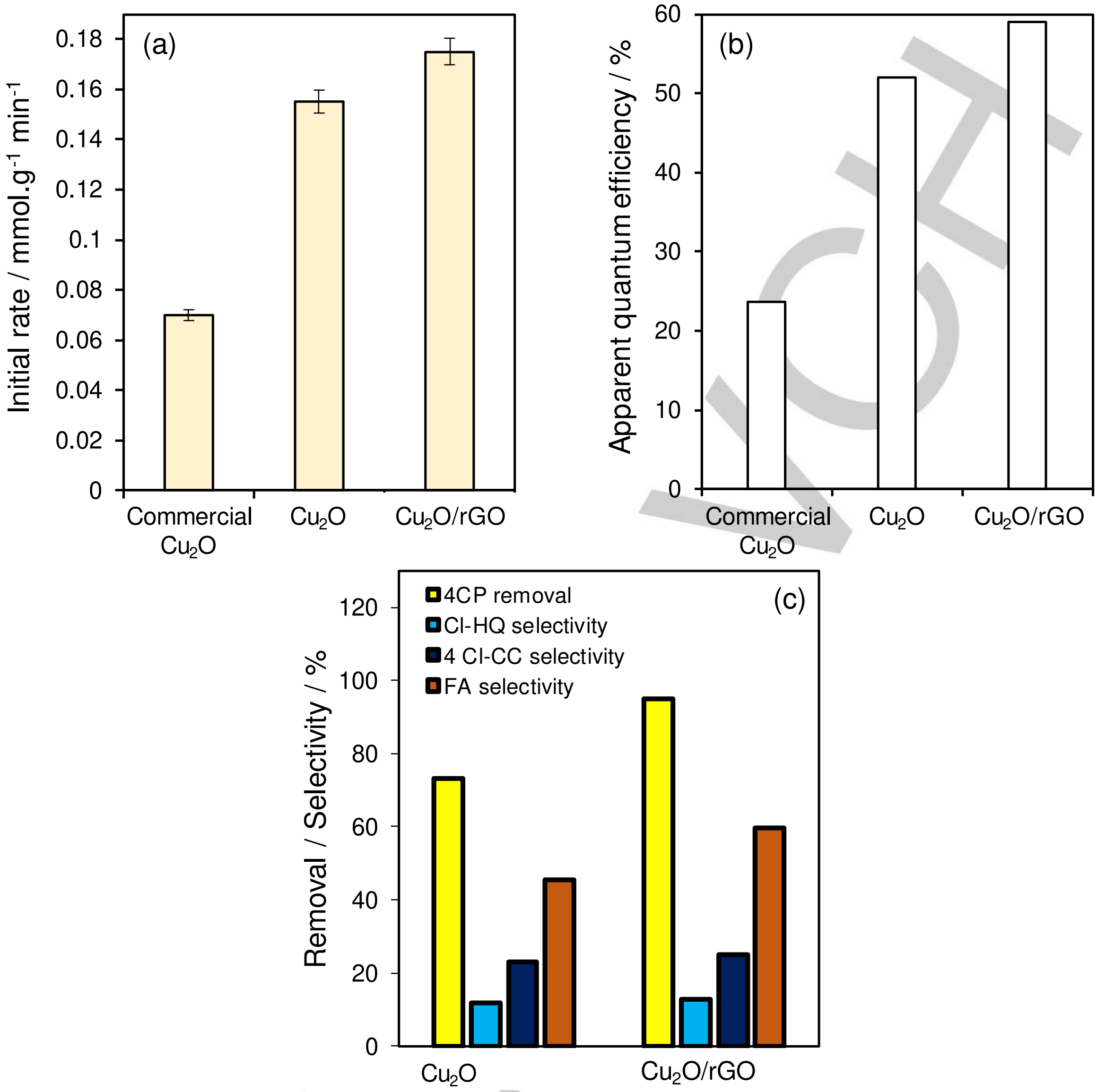

Figure 6. Visible light photocatalytic 4-CP degradation over Pompon Dahlia-like hierarchical Cu_2O and Cu_2O/rGO nanocomposite and commercial Cu_2O nanoparticles: (a) initial rates of 4-CP removal and (b) corresponding apparent quantum efficiencies after 15 min reaction; and (c) 4-CP removal efficiency and product selectivity after 60 min reaction. Experimental conditions: 0.02 g catalyst, 50 mL of 7.78×10^{-5} M aqueous 4-CP, 200 W Hg-Xe arc lamp (λ>420 nm).

light absorption and hence cannot act as a photosensitiser which is problematic in mechanistic investigations of photocatalytic dye degradation.[46] Initial rates and AQE for 4-CP removal (**Figure 6a-b**) by the nanocomposite were slightly higher than for the hierarchical Cu_2O aggregates (0.18 versus 0.16 $mmol.g^{-1}.min^{-1}$, and 59 versus 52 % respectively). However, the conversion of 4-CP reached 95 % for hierarchical Cu_2O/rGO after 60 min reaction, compared with 73 % for the Cu_2O aggregates alone (and only negligible photolysis in the absence of any catalyst), likely associated with increased light absorption. In comparison to both hierarchical catalysts, commercial Cu_2O nanoparticles exhibited poor activity for 4-CP photocatalytic degradation, achieving only 32 % removal after 60 min, attributed to its low surface area (5 $m^2.g^{-1}$ versus 13 $m^2.g^{-1}$ for hierarchical Cu_2O/rGO). There are no reports of 4-CP photodegradation over Cu_2O/rGO photocatalysts, however the present activity far exceeds other semiconductor photocatalysts (**Table 2**), even those employing UV light and/or high power light sources. The initial rate of 4-CP degradation and 1 h removal efficiency showed a modest dependence on rGO loading, with 0.4 wt% rGO exhibiting the optimal performance, however pure rGO was almost inactive (**Figure S7**).

The major products of 4-CP decomposition were chlorohydroquinone (CL-HQ), 4-chlorocatechol (4Cl-CC), and fumaric acid (FA) (**Figure 6c**). Formation of polyoxygenated intermediates is consistent with a radical mechanism involving photogenerated holes transferred to adsorbed water or surface hydroxyls to form hydroxyl radicals (•OH), or the reaction of photoexcited electrons with oxygen to produce •OH via H_2O_2, although direct oxidation of 4-CP cannot be excluded. The hierarchical Cu_2O/rGO favours deeper oxidation and the formation of FA (**Figure 6c**), consistent with more oxidizing equivalents potentially resulting from longer charge carrier lifetimes, and faster charge transfer kinetics (vide infra).[47] Futhermore, Cu_2O/rGO exhibited excellent photostability over five consecutive reactions (**Figure S8**).

Table 2. Comparison of 4-CP removal efficiency over different photocatalysts.

Photocatalyst	Experimental details	Rate constant $10^{-2}.min^{-1}$	Ref.
N-Doped TiO_2	0.1 g catalyst, 500 W Xe lamp (λ>420 nm), 100 mL of 10 mg L^{-1} 4-CP, 180 min.	4.6	59
TiO /WO_3	1.2 g/L catalyst, 50 W lamp (λ>435 nm), $2×10^{-4}$ M 4-CP, 180 min.	0.84	60
TiO_2 – CoPc nanocomposite	0.1 g catalyst, 128 W Lightex LT50 lamp, 100 mL of 0.013 M 4-CP, 30 min.	0.042	61
Combustion synthesized TiO2	1 g/L catalyst, 250 W Xe lamp ($λ_{max}$ 470 nm), 0.15 mmol/L 4-CP, 240 min.	0.049	62
Mesoporous g-C_3N_4	40 mg catalyst, 300 W Xe lamp (λ>420 nm), $1.2 ×10^{-4}$ M 4-CP, 60 min.	5.26	63
Pt/TiO_2	0.5 g/L catalyst, 11 W Hg lamp (λ 200-280 nm), 0.5 mM 4-CP. 120 min.	0.41	64
Heirarchical Cu_2O/rGO	20 mg catalyst, 200 W Hg-Xe arc lamp (λ ≥ 420 nm), 50 mL of $4.2 ×10^{-2}$ mM 4-CP, 60 min.	7.9	This work

The chemical state of copper post-reaction was subsequently investigated. XRD and DRUVS revealed negligible change in the phase or electronic properties of the as-prepared hierarchical Cu_2O/rGO nanocomposite (**Figure S9**), however XPS evidenced an increase in the proportion of surface Cu(II) species (to 60 %) associated with photo-oxidation of the exterior of Cu_2O nanoparticles.

Mechanistic studies

Photocatalytic activity for CO_2 reduction is also reported to increase following the addition of rGO to Cu_2O,[9b] being attributed to increased charge separation across the Cu_2O/rGO interface. Charge separation and recombination effects were investigated in water suspensions using steady state photoluminescence and time-resolved photoluminescence (TRPL) which showed very little difference between Cu_2O and Cu_2O/rGO (**Figure S10a-b**). It is reported that rGO acts as an electron trap in heterojunction nanocomposites,[48] and photoexcited electrons can transfer from the CB of Cu_2O to rGO, leaving photogenerated holes in the Cu_2O VB.[49] TRPL decay curves **(Figure S10b)** were best fit to a bi-exponential function (**Eq. 6**).[50]

$$fit = A + A_1 exp^{\frac{(-t)}{(\tau 1)}} + A_2 exp^{\frac{(-t)}{(\tau 2)}} \qquad \mathbf{6}$$

where, A is the baseline correction constant, t is time, A_1 and A_2 are the contributions of the exponential factors, which include the lifetimes τ_1 and τ_2 of the two excited states. Both lifetimes are short lived consistent with direct radiative emission. The average charge carrier lifetime τ was determined from **Eq. 7**:

$$\tau = A_1\tau 1^2 + A_2\tau 2^2/A_1\tau 1 + A_2\tau 2 \qquad \mathbf{7}$$

and shows that photoinduced charge carrier lifetimes are essentially identical for the Cu_2O/rGO nanocomposite and hierarchical Cu_2O (**Table 3**). We therefore find no evidence for significant interfacial charge separation across the heterojunction.[51]

Table 3. TRPL fitting of Pompon Dahlia-like hierarchical Cu_2O and Cu_2O/rGO nanocomposite.

Photocatalyst	τ_1 / ns	τ_2 / ns	$A_1/(A_1+A_2)$ / %	$A_2/(A_1+A_2)$ / %	τ / ns	χ^2
Hierarchical Cu_2O	1.601	2.056	23.6	76.4	1.97	1.441
Hierarchical Cu_2O/rGO	1.662	2.251	23.0	77.0	2.14	1.314

Photoelectrochemical measurements showed transient photocurrents (**Figure 7a**) of the Cu_2O/rGO composite was approximately double that of the Cu_2O aggregates indicating more redox equivalents are available for photocatalytic reactions. Electrochemical impedance spectroscopy can also provide insight into photoelectrode phenomena. Ideally, an equivalent circuit can be found to model specific photophysical and photoelectrochemical phenomena. More generally, the radius of the impedance curve on a resulting Nyquist plot reflects the resistance in the system. Comparison of data acquired in the dark and under illumination show the reduced radius of the lower frequency feature of the Cu_2O/rGO nanocomposite under illumination (**Figure 7b**) indicating that the introduction of rGO facilitates electron migration across the electrode or at the electrode/electrolyte interface.[52] Corresponding Mott Schottky plots under illumination (**Figure 7c**) provide insight into the flat band potential and doping density. Negative slopes were obtained for the hierarchical Cu_2O and Cu_2O/rGO nanocomposite, consistent with p-type semiconductors. The x-axis intercept shows the flat band potentials of Cu_2O and Cu_2O/rGO nanocomposite are similar at around 1.1 V and 0.98 V, respectively, which compares to 0.55 V reported for a continuous film of cubic Cu_2O nanocrystals.[52] A more positive flat band potential will increase the rate of oxidation of MeOH and water, supporting H_2 production and 4-CP degradation, respectively (**Figure 5** and **6**). The slope of the linear portion of the curve in a

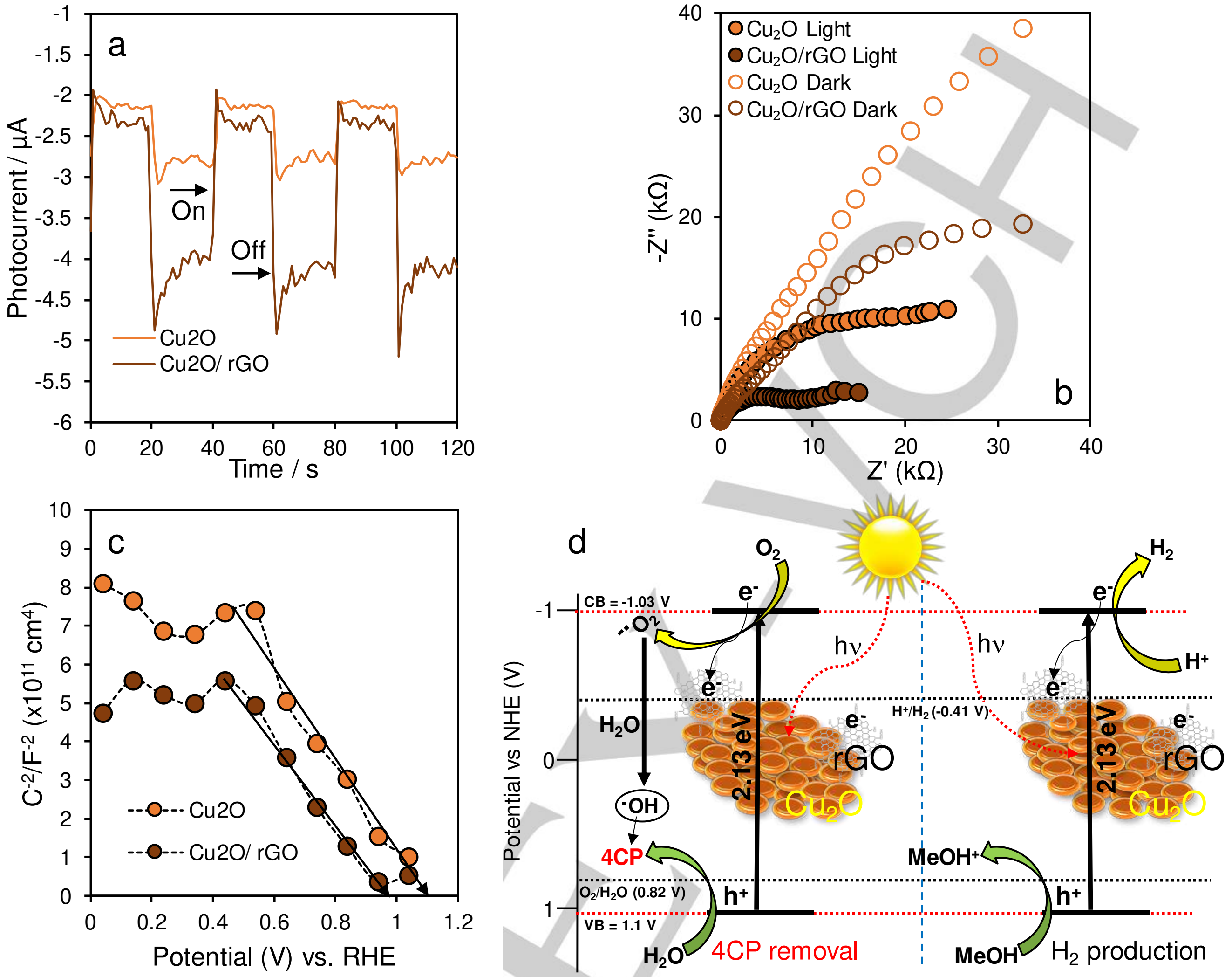

Figure 7. (a) Transient photocurrent, (b) EIS (Nyquist) plot at 0 V vs. RHE, (c) Mott-Schottky plot of Cu_2O, Cu_2O/rGO, and Cu_2O/rGO (200 W Hg-Xe arc lamp and 0.5 M $NaSO_4$ electrolyte), and (d) proposed charge transfer mechanism for Cu_2O/rGO.

Mott-Schottky plot is used to calculate the majority carrier density from **Eq. 8**:

$$\frac{1}{C^2}=\frac{2}{\varepsilon\varepsilon_0 e N_A}\left(V-E_{fb}-\frac{k_BT}{e}\right) \qquad \textbf{8}$$

where ε is the dielectric constant (7.60 for Cu_2O[53]), ε_0 is the permittivity of free space, e is the electron charge, N_A is the majority carrier density, V is the applied potential, $E_{fb}$is the flat band potential, k_B is the Boltzmann's constant and T is the temperature. The majority carrier densities were similar at 1.5 x 10^{19} cm^{-3} and 1.7 x 10^{19} cm^{-3} for hierarchical Cu_2O and Cu_2O/rGO respectively, both higher that for Cu_2O (3.07 x 10^{17} cm^{-3}), CuO (2.41 x10^{18} cm^{-3}), and Cu_2O/CuO bilayered composite (2.58 x10^{18} cm^{-3}) photoanodes prepared by thermal oxidation[52], though less than for electrodeposited/annealed p-type Cu_2O-CuO thin films[54] (at 1.3 x 10^{20} cm^{-3}). Together with the similar flat band potentials, these values suggest there is little difference in either charge transfer rates or the driving force for charge separation between our two catalysts (in contrast to Cu_2O/CuO bilayered composites[52]). Hence the higher photoactivity of the hierarchical Cu_2O/rGO nanocomposite for hydrogen production and 4-CP degradation compared to hierarchical Cu_2O appears solely associated with its broader absorption of visible light, and not reduced recombination.

A tentative mechanism for photocatalytic 4-CP oxidative degradation over the hierarchical Cu_2O/rGO nanocomposite is illustrated in **Scheme 2**. Under illumination, electrons (e^-) within the Cu_2O valence band are photoexcited into the Cu_2O conduction band, and subsequently migrate to rGO sheets. Resulting Cu_2O valence band holes (h^+) may then react with hydroxyl ions from the aqueous solution to form •OH radicals, while photoexcited electrons trapped by rGO react with dissolved oxygen to form superoxide $O_2^{-\bullet}$ radicals. The latter may further react with water to produce additional •OH through redox reactions. Reactive intermediates identified by HPLC included chlorohydroquinone (Cl-HQ), chlorocatechol (Cl-CC) and fumaric acid (FA), indicating that the 4-CP photooxidation pathway processes according to **Scheme 2**, with OH• radicals the key oxidant (**Eqs. 9-15**).

$$Cu_2O/rGO + hv \rightarrow Cu_2O/rGO^*(h_{VB}^{+} + e_{CB}^{-}) \quad 9$$

$$Cu_2O/rGO^*\ (h_{VB}^{+}) + H_2O \rightarrow Cu_2O/rGO\ (HO^{\cdot}) + H^{+} \quad 10$$

$$Cu_2O/rGO^*(e_{CB}^{-}) + O_2 \ \rightarrow Cu_2O/rGO(O_2^{-\cdot}) \quad 11$$

$$Cu_2O/rGO(O_2^{-\cdot}) + H^{+} \rightarrow Cu_2O/rGO^*(HO_2^{\cdot}) \quad 12$$

$$Cu_2O/rGO^*(HO_2^{\cdot}) + Cu_2O/rGO^*(HO_2^{\cdot}) \rightarrow Cu_2O/rGO(H_2O_2) + O_2 \quad 13$$

$$Cu_2O/rGO(H_2O_2) + hv \rightarrow Cu_2O/rGO^*(2HO^{\cdot}) \quad 14$$

$$Cu_2O/rGO^*(HO^{\cdot}) + {\scriptstyle 4CP} + hv \rightarrow Reactive\ intermediates + H_2O \quad 15$$

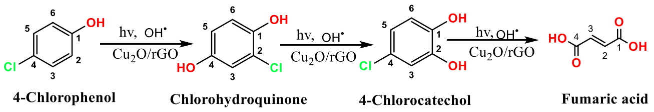

Scheme 2. Proposed 4-CP photodegradation pathway.

Conclusions

A hierarchical Cu_2O/rGO nanocomposite was fabricated by electrostatic self-assembly and subsequent low temperature hydrothermal processing. The resulting nanocomposite comprised 300-500 nm aggregates of 15-30 nm Cu_2O nanocrystals arranged in a Pompom Dahlia (flower)-like structure, in contact with 1 wt% of rGO nanosheets. This architecture offers broad visible light absorption and excellent stability, resulting in high activity for photocatalytic H_2 production from water-alcohol, and 4-CP degradation predominantly to (low toxicity) fumaric acid, without recourse to precious metal co-catalysts. Such hierarchical Cu_2O/rGO nanocomposites may provide a low cost approach to solar fuels and chemical (via CO_2 reduction) production, and the environmental remediation of recalcitrant wastewater pollutants.

Experimental Section

Chemicals: Copper (II) chloride ($CuCl_2$, 97 %, Aldrich), polyethylene glycol (Alfa Aesar, MW600), sodium hydroxide (NaOH, Sigma), hydrazine monohydrate ($H_4N_2.H_2O$, Alfa Aesar, 98 %), ethanol (Fisher chemicals, 9.8 %), rGO (Sigma), Cu_2O nanoparticles (Sigma, 97 %, 5000 nm particle size, 47 nm crystallite size, 5 $m^2.g^{-1}$), 4-chlorophenol (C_6H_5ClO, Acros organics, 99 %), chlorohydroquinone (Sigma, 85 %) Chlorocatechol (Sigma, 97 %), fumaric acid (Sigma, 99 %), sodium sulfate (Na_2SO_4, Sigma, 99 %), sodium sulfite (Na_2SO_3, Sigma, 98 %), potassium bromide (KBr, Sigma, 99 %), Nafion (Sigma), H_2O HPLC grade (Sigma), and acetonitrile HPLC grade (Sigma, 99.93 %) were used without purification. Deionised water was used for all solutions.

Synthesis of hierarchical Cu_2O/rGO: A Pompon Dahlia (flower)-like Cu_2O/rGO catalyst was synthesised by solution phase chemistry under ambient conditions. GO (2 mg) prepared following a literature method[55] was ultrasonicated in 10 mL water for 30 min, to which a mixture of 50 mL of 0.2 M copper chloride and 5 mL of 0.06 M PEG-600 was added and followed by a further 10 min ultrasonication. The resulting mixture was then heated to 60 °C under stirring for 30 min, resulting in a deep blue solution. Subsequently, 8 mL of 2 M NaOH was added into the preceding deep blue solution, and followed by the dropwise addition of 1 M aqueous hydrazine monohydrate ($H_4N_2.H_2O$) (1 mL in 5 mL of water) under stirring for an additional 5 min. The reaction mixture was then transferred to 20 mL cold water in a multi-neck round-bottomed flask and purged under N_2 for 30 min to promote the formation of Cu_2O (brownish-yellow colour change). The resulting solid was separated from the reaction mixture by centrifugation at 6000 rpm for 10 min, washed with H_2O and then ethanol to remove residual PEG, and finally vacuum dried for 24 h and stored in a vacuum desiccator. Cu_2O is formed through the initial complexation of Cu(II) ions with PEG and rGO, and subsequent precipitation as the Cu(I) oxide by hydrazine reduction in the presence of NaOH. Hydroxyl groups from PEG and rGO likely play an important role in controlling the Cu(II) ion density and directing the formation of hierarchical Cu_2O structures. The preceding synthesis corresponds to a nominal rGO mass loading of 0.4 % in the hierarchical Cu_2O/rGO nanocomposite, and was extended to prepare nanocomposites with nominal rGO mass loadings spanning 2-100 %, and in the absence of GO to prepare pure Dahlia (flower)-like Cu_2O with morphologies akin to those reported by Kow et al.[56] In all cases the final catalysts were a reddish-orange colour, produced in ~540 mg yield, and exhibited essentially identical electronic and crystalline properties (**Figure S11**), although high rGO loadings result in encapsulation of Cu_2O nanoparticles (**Figure S12**) which may hinder photoexcitation and 4-CP adsorption by the metal oxide.

Physicochemical characterization: Crystallinity and phase indexing was performed by powder X-ray diffraction (XRD) using a Bruker-AXS D8 ADVANCE diffractometer operated at 40 kV and 40 mA and Cu Kα radiation (λ=0.15418 nm) between 2θ 10-80° in 0.02° steps. X-ray photoelectron spectroscopy (XPS) was undertaken on a Kratos Axis HSi spectrometer with monochromated Al Kα X-ray source operated at 90 W and normal emission, with magnetic focusing and a charge neutraliser. Spectra were fitted using CasaXPS version 2.3.16, with energy referencing to adventitious carbon at 284.6 eV, and surface compositions derived through applying appropriate instrumental response factors. TEM microscopy was performed on a JEM-2100Plus microscope operated at 200 kV (Warwick University, UK); samples were dispersed in ethanol and ultrasonicated for 5 min and then drop coated on Cu grid coated with carbon film. Brunauer–Emmett-Teller (BET) surface areas were obtained by N2 physisorption at 77 K using a Quantachrome NOVA 4000e porosimeter on samples degassed at 120 °C for 4 h. Surface areas were calculated over the relative pressure range 0.01-0.2, and BJH pore size distributions calculated from the desorption branch of the isotherm for relative pressures >0.35. Diffuse reflectance UV-vis absorption spectra (DRUVS) were recorded on a Thermo Scientific Evo220 spectrometer using an integrating sphere, and KBr as a standard, with band gaps determined between 200-800 nm. Steady state photoluminescence (PL) spectra were measured on a F-4500FL spectrophotometer using 560 nm excitation. Time-resolved photoluminescence (TRPL) spectra were measured on an Edinburgh Photonics FLS 980 spectrometer using pulsed picosecond LED light and 560 nm excitation.

Photoelectrochemical characterization: A three electrode photoelectrochemical cell was used, comprising a Pt wire counter electrode and Hg/Hg_2SO_4 reference electrode. The photoelectrochemical measurements were converted to the reversible hydrogen electrode (RHE) using **Eq. 1:**

$$\mathrm{E}_{V\ vs.\ RHE} = \mathrm{E}_{V\ vs.\ \frac{Hg}{Hg_2SO_4}} + \mathrm{E}_{\frac{Hg}{Hg_2SO_4}} + 0.059\ p \qquad \mathbf{1}$$

The working electrode was prepared by dropcasting 5 µL of a homogeneous colloidal suspension on a 3 mm diameter glassy carbon electrode. The colloid was prepared by 30 min sonication of a catalyst and Nafion dispersed in a water/ethanol mixture (0.5 mL, 1:1 v/v). Nitrogen degassed 0.5 M Na_2SO_4 was used as the electrolyte with a pH of 6.8. Irradiation was performed using a 200 W Hg-Xe arc lamp ((Oriel Instruments 66002, λ>420 nm). Nyquist plots were recorded under illumination and in the dark on an Autolab potentiostat with Nova software using a 10 mV AC signal applied between 100 kHz to 0.1 Hz, and Mott-Schottky plots were recorded at 1000 Hz (under illumination and in the dark) using a DC signal spanning -1 to 0 V in 10 mV potential steps.

Photocatalytic H_2 evolution: Photocatalytic H_2 production was performed using hierarchical Cu_2O and Cu_2O/rGO photocatalysts in a sealed quartz photoreactor (384 mL volume) with a 200 W Hg-Xe arc lamp (Oriel Instruments 66002) and 420 nm cut-off filter to remove UV light; the light intensity inside the reactor was 43.7 mW.cm^{-2}. Catalysts (20 mg) were dispersed in 45 mL water with 5mL methanol as a sacrificial hole scavenger and sonicated for 5 min to obtain a uniform distribution. The photoreactor was then purged with He for 1 h in the dark to remove dissolved oxygen, prior to visible light irradiation. Aliquots of gas from the reactor headspace were periodically withdrawn during irradiation using a 1 mL gas syringe and injected into a Shimadzu Tracera GC-2010 Plus gas chromatography fitted with a Carboxen1010 capillary column (30 m×0.53 mm×0.1 µm) and barrier ionization detector (using a He carrier) for gas analysis. Mass-normalised photocatalytic activities are reported to enable quantitative benchmarking of different catalysts, as described in the literature.[57]

4-CP photocatalytic degradation: Photocatalytic 4-CP degradation was performed in a sealed quartz photoreactor (260 mL) using a 200 W Hg-Xe arc lamp with 420 nm cut-off filter, and the temperature maintained at 25 °C by a Huber Minichiller. Catalysts (20 mg) were dispersed in 50 mL of 7.78×10^{-5} M aqueous 4-CP solution by 7 min ultrasonication in the dark and stirred for a subsequent 120 min in the dark to equilibrate molecular adsorption. Aliquots (1 mL) were periodically withdraw from the reaction mixture for HPLC analysis. Post-reaction catalysts were separated by centrifugation at 8000 rpm for 10 min, and then vacuum dried and stored in a vacuum desiccator for characterisation. The catalyst mass was selected to enable measurement of intrinsic reaction kinetics (**Figure S13**). Concentrations of 4-CP and chlorohydroquinone (Cl-HQ), 4-chlorocatechol (4Cl-CC) and fumaric acid (FA) products were determined from multi-point calibration curves of reference compounds using an Agilent 1260 Infinity Quaternary HPLC equipped with UV diode array and refractive index detectors; an Agilent Zorbax Eclipse plus C18 column was employed at 35 °C using 1 mL/min of a 30 vol% acetonitrile/70 vol% water (HPLC grade) mobile phase, and 280 nm detection. The extent of 4-CP removal, and product selectivity's were calculated from **Eqs. 2 and 3** respectively:

$$\%\ \text{4CP removal} = \frac{4\text{CP}_{initial} - 4\text{CP}_{final}}{4\text{CP}_{initial}} \times 100 \qquad \mathbf{2}$$

where, the 4CP$_{initial}$ and 4CP$_{final}$ are the mols of 4-CP at the start and end of the irradiation period.

$$\%\ \text{Selectivity} = \frac{\text{mols Product}}{\left(4\text{CP}_{initial} - 4\text{CP}_{final}\right)} \times 100 \qquad \mathbf{3}$$

Acknowledgements

We thank the Royal Society and Science and Engineering Research Board for the award of a Royal Society-SERB "Newton International Fellowship (NF NF151399)" to S.K. We thank the Biotechnology and Biological Sciences Research Council (BBSRC; via grant BB/P022685/1). S. K. and K. S. would like to thank the Japan Society for the Promotion of Science (JSPS) for providing a postdoctoral fellowship for foreign researchers (P18387) and the research grant (KAKENHI JP18F18387).

Keywords: Cu_2O • reduced graphene oxide • 4-chlorophenol • hydrogen • photocatalysis

[1] R. D. Cortright, R. R. Davda, J. A. Dumesic, *Nature* **2002**, *418*, 964.
[2] Y. Hou, B. L. Abrams, P. C. K. Vesborg, M. E. Björketun, K. Herbst, L. Bech, A. M. Setti, C. D. Damsgaard, T. Pedersen, O. Hansen, J. Rossmeisl, S. Dahl, J. K. Nørskov, I. Chorkendorff, *Nat. Mater.* **2011**, *10*, 434.
[3] a) F. Fresno, R. Portela, S. Suárez, J. M. Coronado, *J. Mat. Chem. A* **2014**, *2*, 2863-2884; b) M. A. Fox, M. T. Dulay, *Chem. Rev.* **1993**, *93*, 341-357.
[4] P. D. Tran, L. H. Wong, J. Barber, J. S. Loo, *Energy Environ. Sci.* **2012**, *5*, 5902-5918.
[5] a) J. Ran, J. Zhang, J. Yu, M. Jaroniec, S. Z. Qiao, *Chem. Soc. Rev.* **2014**, *43*, 7787-7812; b) H. Wang, L. Zhang, Z. Chen, J. Hu, S. Li, Z. Wang, J. Liu, X. Wang, *Chem. Soc. Rev.* **2014**, *43*, 5234-5244.
[6] M. Heinemann, B. Eifert, C. Heiliger, *Phys. Rev. B* **2013**, *87*, 115111.
[7] M. Hara, T. Kondo, M. Komoda, S. Ikeda, J. N. Kondo, K. Domen, M. Hara, K. Shinohara, A. Tanaka, *Chem. Commun.* **1998**, 357-358.
[8] J. Luo, L. Steier, M.-K. Son, M. Schreier, M. T. Mayer, M. Grätzel, *Nano Lett.* **2016**, *16*, 1848-1857.
[9] a) A. Chakravarty, K. Bhowmik, A. Mukherjee, G. De, *Langmuir* **2015**, *31*, 5210-5219; b) X. An, K. Li, J. Tang, *ChemSusChem* **2014**, *7*, 1086-1093; c) R. Chen, S. Pang, H. An, J. Zhu, S. Ye, Y. Gao, F. Fan, C. Li, *Nat. Energy* **2018**, *3*, 655.
[10] A. S. Zoolfakar, R. A. Rani, A. J. Morfa, A. P. O'Mullane, K. Kalantar-Zadeh, *J. Mat. Chem. C* **2014**, *2*, 5247-5270.
[11] S. Sahoo, S. Husale, B. Colwill, T.-M. Lu, S. Nayak, P. M. Ajayan, *ACS Nano* **2009**, *3*, 3935-3944.
[12] W. Z. Wang, G. Wang, X. S. Wang, Y. Zhan, Y. Liu, C. L. Zheng, *Adv. Mater.* **2002**, *14*, 67-69.
[13] W.-C. Huang, L.-M. Lyu, Y.-C. Yang, M. H. Huang, *J. Am. Chem. Soc.* **2011**, *134*, 1261-1267.
[14] S. Jiao, L. Xu, K. Jiang, D. Xu, *Adv. Mater.* **2006**, *18*, 1174-1177.
[15] H. Xu, W. Wang, *Angew. Chem. Int. Ed.* **2007**, *46*, 1489-1492.
[16] S. Karthikeyan, S. Kumar, L. J. Durndell, M. A. Isaacs, C. M. Parlett, B. Coulson, R. E. Douthwaite, Z. Jiang, K. Wilson, A. F. Lee, *ChemCatChem* **2018**, *10*, 3554-3563.
[17] C. M. A. Parlett, K. Wilson, A. F. Lee, *Chem. Soc. Rev.* **2013**, *42*, 3876-3893.
[18] S. Kumar, C. M. Parlett, M. A. Isaacs, D. V. Jowett, R. E. Douthwaite, M. C. Cockett, A. F. Lee, *Appl. Catal. B-Environ.* **2016**, *189*, 226-232.
[19] H. Zhang, Q. Zhu, Y. Zhang, Y. Wang, L. Zhao, B. Yu, *Adv. Funct. Mater.* **2007**, *17*, 2766-2771.
[20] a) L. Chen, Y. Zhang, P. Zhu, F. Zhou, W. Zeng, D. D. Lu, R. Sun, C. Wong, *Sci. Rep.* **2015**, *5*, 9672; b) L. Zhang, P. Ying, B. Yu, L. Wu, J. Wang, X. Gu, S. Chen, R. Zhou, Z. Ni, *RSC. Adv.* **2014**, *4*, 42892-42898.

[21] M. Hartmann, *Angew. Chem. Int. Ed.* **2004**, *43*, 5880-5882.

[22] a) K. S. Novoselov, A. K. Geim, S. V. Morozov, D. Jiang, Y. Zhang, S. V. Dubonos, I. V. Grigorieva, A. A. Firsov, *Science* **2004**, *306*, 666-669; b) A. K. Geim, K. S. Novoselov, *Nat. Mater.* **2007**, *6*, 183.

[23] F. Li, L. Zhang, J. Tong, Y. Liu, S. Xu, Y. Cao, S. Cao, *Nano Energy* **2016**, *27*, 320-329.

[24] a) Y. Liang, Y. Li, H. Wang, J. Zhou, J. Wang, T. Regier, H. Dai, *Nat. Mater.* **2011**, *10*, 780; b) Q. Xiang, J. Yu, *J. Phys. Chem. Lett.* **2013**, *4*, 753-759; c) Q. Xiang, B. Cheng, J. Yu, *Angew. Chem. Int. Ed.* **2015**, *54*, 11350-11366.

[25] Z. Gan, X. Wu, M. Meng, X. Zhu, L. Yang, P. K. Chu, *ACS Nano* **2014**, *8*, 9304-9310.

[26] Z. Zhang, R. Dua, L. Zhang, H. Zhu, H. Zhang, P. Wang, *ACS Nano* **2013**, *7*, 1709-1717.

[27] C. K. Chua, M. Pumera, *Chem. Commun.* **2016**, *52*, 72-75.

[28] W. Wang, P. Zhang, L. Peng, W. Xie, G. Zhang, Y. Tu, W. Mai, *CrystEngComm* **2010**, *12*, 700-701.

[29] S. Liu, Z. Chen, N. Zhang, Z.-R. Tang, Y.-J. Xu, *J. Phys. Chem. C* **2013**, *117*, 8251-8261.

[30] S. Sun, X. Zhang, X. Song, S. Liang, L. Wang, Z. Yang, *CrystEngComm* **2012**, *14*, 3545-3553.

[31] a) Q. Li, B. Guo, J. Yu, J. Ran, B. Zhang, H. Yan, J. R. Gong, *J. Am. Chem. Soc.* **2011**, *133*, 10878-10884; b) J. T.-W. Wang, J. M. Ball, E. M. Barea, A. Abate, J. A. Alexander-Webber, J. Huang, M. Saliba, I. Mora-Sero, J. Bisquert, H. J. Snaith, R. J. Nicholas, *Nano Lett.* **2014**, *14*, 724-730.

[32] W. Zou, L. Zhang, L. Liu, X. Wang, J. Sun, S. Wu, Y. Deng, C. Tang, F. Gao, L. Dong, *Appl. Catal. B-Environ.* **2016**, *181*, 495-503.

[33] C. H. Kuo, C. H. Chen, M. H. Huang, *Adv. Funct. Mater.* **2007**, *17*, 3773-3780.

[34] A. Al Nafiey, A. Addad, B. Sieber, G. Chastanet, A. Barras, S. Szunerits, R. Boukherroub, *Chem. Eng. J.* **2017**, *322*, 375-384.

[35] J. Liu, J. Ke, D. Li, H. Sun, P. Liang, X. Duan, W. Tian, M. O. Tadé, S. Liu, S. Wang, *ACS Appl. Mater. Interfaces* **2017**, *9*, 11678-11688.

[36] Y. Chang, J. J. Teo, H. C. Zeng, *Langmuir* **2005**, *21*, 1074-1079.

[37] S. Deng, V. Tjoa, H. M. Fan, H. R. Tan, D. C. Sayle, M. Olivo, S. Mhaisalkar, J. Wei, C. H. Sow, *J. Am. Chem. Soc.* **2012**, *134*, 4905-4917.

[38] L. Xu, F. Zhang, X. Song, Z. Yin, Y. Bu, *J. Mat. Chem. A* **2015**, *3*, 5923-5933.

[39] Y. Xu, A. Li, T. Yao, C. Ma, X. Zhang, J. H. Shah, H. Han, *ChemSusChem* **2017**, *10*, 4277-4305.

[40] M. Singh, D. Jampaiah, A. E. Kandjani, Y. M. Sabri, E. Della Gaspera, P. Reineck, M. Judd, J. Langley, N. Cox, J. van Embden, E. L. H. Mayes, B. C. Gibson, S. K. Bhargava, R. Ramanathan, V. Bansal, *Nanoscale* **2018**, *10*, 6039-6050.

[41] a) G. Nagabhushana, G. Nagaraju, G. Chandrappa, *J. Mat. Chem. A* **2013**, *1*, 388-394; b) S. Karthikeyan, S. Kumar, L. J. Durndell, M. A. Isaacs, C. M. A. Parlett, B. Coulson, R. E. Douthwaite, Z. Jiang, K. Wilson, A. F. Lee, *ChemCatChem* **2018**, *10*, 3554-3563.

[42] D. Mateo, I. Esteve-Adell, J. Albero, A. Primo, H. García, *Appl. Catal. B-Environ.* **2017**, *201*, 582-590.

[43] S. Kakuta, T. Abe, *Electrochem. Solid State Lett.* **2009**, *12*, P1-P3.

[44] S. Kumar, C. M. A. Parlett, M. A. Isaacs, D. V. Jowett, R. E. Douthwaite, M. C. R. Cockett, A. F. Lee, *Appl. Catal. B-Environ.* **2016**, *189*, 226-232.

[45] D. Barreca, P. Fornasiero, A. Gasparotto, V. Gombac, C. Maccato, T. Montini, E. Tondello, *ChemSusChem* **2009**, *2*, 230-233.

[46] N. Barbero, D. Vione, *Environ. Sci. Technol.* **2016**, *50*, 2130-2131.

[47] Y. Li, Z. Sun, S. Zhu, Y. Liao, Z. Chen, D. Zhang, *Carbon* **2015**, *94*, 599-606.

[48] a) G. Katsukis, J. Malig, C. Schulz-Drost, S. Leubner, N. Jux, D. M. Guldi, *ACS Nano* **2012**, *6*, 1915-1924; b) Y. Hou, A. B. Laursen, J. Zhang, G. Zhang, Y. Zhu, X. Wang, S. Dahl, I. Chorkendorff, *Angew. Chem. Int. Ed.* **2013**, *52*, 3621-3625; c) P. N. O. Gillespie, N. Martsinovich, *ACS Appl. Mater. Interfaces* **2019**, *11*, 31909-31922.

[49] Y.-C. Pu, H.-Y. Chou, W.-S. Kuo, K.-H. Wei, Y.-J. Hsu, *Appl. Catal. B-Environ.* **2017**, *204*, 21-32.

[50] a) S. Cao, Q. Huang, B. Zhu, J. Yu, *J. Power Sources* **2017**, *351*, 151-159; b) M. Athanasiou, R. Smith, B. Liu, T. Wang, *Sci. Rep.* **2014**, *4*, 7250.

[51] D. K. Padhi, K. Parida, *J. Mat. Chem. A* **2014**, *2*, 10300-10312.

[52] Y. Yang, D. Xu, Q. Wu, P. Diao, *Sci. Rep.* **2016**, *6*, 35158.

[53] Z. Zhang, P. Wang, *J. Mat. Chem.* **2012**, *22*, 2456-2464.

[54] P. Wang, H. Wu, Y. Tang, R. Amal, Y. H. Ng, *J. Phys. Chem. C* **2015**, *119*, 26275-26282.

[55] W.-K. Jo, S. Kumar, M. A. Isaacs, A. F. Lee, S. Karthikeyan, *Appl. Catal. B-Environ.* **2017**, *201*, 159-168.

[56] J. Kou, A. Saha, C. Bennett-Stamper, R. S. Varma, *Chem. Commun.* **2012**, *48*, 5862-5864.

[57] a) T. Maschmeyer, M. Che, *Angewandte Chemie International Edition* **2010**, *49*, 1536-1539; b) T. Maschmeyer, M. Che, *Angewandte Chemie International Edition* **2010**, *49*, 9590-9591; c) H. Kisch, *Angewandte Chemie International Edition* **2010**, *49*, 9588-9589.

Entry for the Table of Contents

FULL PAPER

Text for Table of Contents

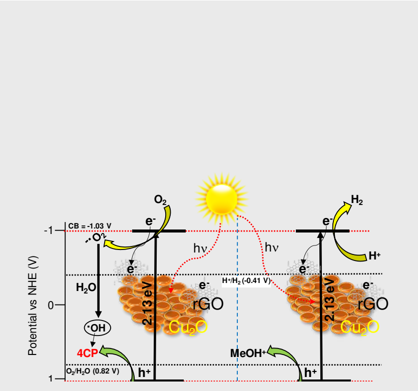

*Author(s), Corresponding Author(s)**

Page No. – Page No.

Title